



1 Gridded surface O₃, NO_x, and CO abundances for model metrics from the South Korean ground station network

2 Calum P. Wilson¹, Michael J. Prather¹

3 ¹Department of Earth System Science, University of California (Irvine), Irvine, CA 92697, USA

4 *Correspondence to:* Calum P. Wilson (calumw@uci.edu)

5 **Abstract.** We present gridded surface air quality datasets over South Korea for three key species – ozone (O₃), carbon
6 monoxide (CO), and nitrogen oxides (NO_x) during the timeframe of the Korea–US Air Quality (KORUS–AQ) mission (May–
7 June 2016). The tenth degree hourly averaged abundances are constructed from the 300+ air quality network sites using inverse
8 distance weighting with simple declustering. Cross–comparing the interpolated fields against the site data that was used to
9 create them reveals high prediction skill for O₃ (80%) throughout South Korea, and moderate skill (60%) for CO and NO_x on
10 average in densely observed regions after individual mean bias corrections. The gridded O₃ and CO interpolations predict the
11 NASA DC–8 observations in the planetary boundary layer (PBL) with high skill (80%) in the Seoul Metropolitan Area (SMA)
12 after subtracting the mean bias. DC–8 NO_x observations were much less predictable on account of consistently negative vertical
13 gradients within the PBL. Our gridded products capture the mean and variability of O₃ throughout South Korea, and of CO
14 and surface NO_x in most site–dense urban centres (SMA, Cheongju, Gwangju, Daegu, Changwon, and Busan).

15 1 Introduction

16 Air quality control has become a priority in the Republic of Korea following an upward trend in ozone (O₃) pollution in all
17 major cities since the 1980s (Susaya et al., 2013). In May–June 2016, the Korea–US Air Quality (KORUS–AQ) mission was
18 launched with the goal of improving knowledge of the factors controlling Korean air pollution; this mission gathered extensive
19 observational data via aircraft, ground stations, ships, and remote sensing (Crawford et al., 2021).

20 Comparisons of modelled grid–cell values (i.e., averages) with point data from station sites remains awkward,
21 especially in high–emission environments with high sub–grid and temporal variability. Ground site comparisons in South
22 Korea have thus far used the arithmetic mean of sites within a grid cell or ungridded quantile analysis (Lennartson et al., 2018;
23 Peterson et al., 2019; Eck et al., 2020; Jordan et al., 2020; Schroeder et al., 2020; Park et al., 2021; Oak et al., 2022; Travis et
24 al., 2022), but these unweighted means can be biased by site clustering, and they lose information outside the cells. In this
25 work we develop a gridded dataset of key surface–level pollutants (in this case, O₃, NO_x, CO) observed during the KORUS–
26 AQ timeframe. In contrast to arithmetic means, we apply Inverse Distance Weighting (IDW) interpolations (Shepard, 1968)
27 improved by Schnell et al. (2014) to create a country–wide continuous mapping of the National Institute of Environmental
28 Research (NIER) ground site data. We subsequently integrate the interpolated field over a 0.1°x0.1° grid. To evaluate the
29 interpolation, we predict NIER station measurements using the leave–one–out cross validation method; we predict



30 observations from two research sites (Olympic Park and Taehwa Forest) to verify instrumental cohesion; and, we compare our
31 gridded fields with DC–8 observations within the planetary boundary layer (PBL) to gauge how well the data products
32 reproduce upper PBL abundances. In addition to providing gridded PBL datasets, we discuss the applicability and limitations
33 of our methodology for each key species.

34 The observational data sets are described in Section 2, and the methods in Section 3. Results are summarized in
35 Section 4. Conclusions and recommendations are presented in Section 5.

36 **2 KORUS–AQ data**

37 All the KORUS–AQ datasets introduced in this section are publicly available via
38 <https://doi.org/10.5067/Suborbital/KORUSAQ/DATA01>.

39 **2.1 NIER air quality stations**

40 The AirKorea monitoring network (<https://www.airkorea.or.kr/eng>) provided ground measurements of the key species
41 averaged every 5 minutes at 323 stations across South Korea, of which 319 reported O₃, 311 reported CO, and 321 reported
42 NO_x (Fig. 1). We calculate hourly median readings centred on the hour for each station, but discard clearly erroneous O₃ and
43 NO_x dropouts. These dropouts are manifest as stably low concentrations (1–4 ppb) persisting for multiple hours in stark contrast
44 with the typical variability at the site. We were able to flag most dropouts algorithmically by analyzing the cumulative density
45 functions (CDFs) of the station data partitioned into non–overlapping weekly intervals; improbably frequent low data often
46 featured flat empirical gradients (less than 100th of the median CDF gradient) at the tail of the CDF. This technique proved
47 insufficient at some stations however, and so we manually removed dropouts that were not flagged by our algorithm, as did
48 Eck et al, 2020. The NIER instruments and procedures are not well documented and there remain some oddities: CO was
49 reported with 1 ppb precision at 68 sites, and with 100 ppb precision at the remaining 250 sites.

50 **2.2 Research stations**

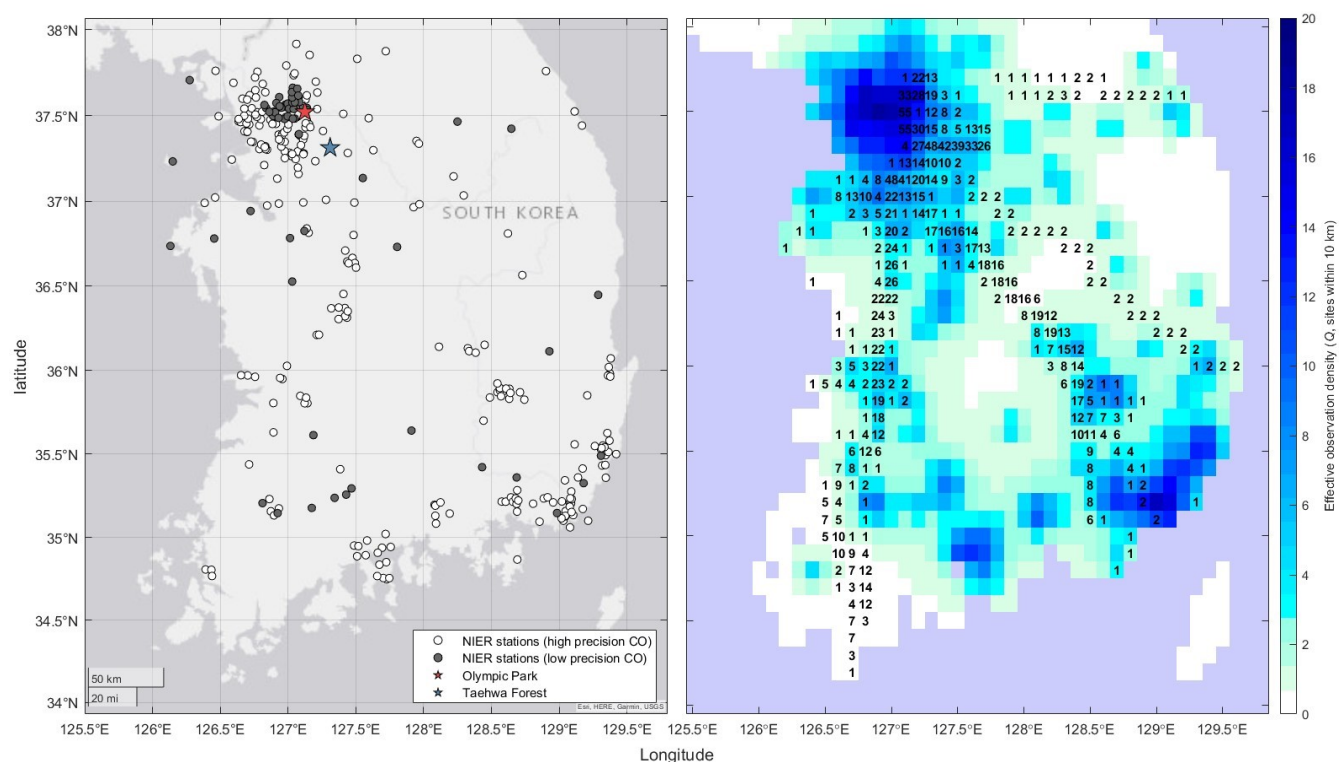
51 **2.2.1 Olympic Park**

52 The Olympic Park research station lies at the southeast edge of Seoul at 37.5216°N, 127.1242°E, 30 m above sea level, and
53 served as a reference for ground–level Seoul pollution during the KORUS–AQ campaign (red star in Fig. 1). Hourly averages
54 for the key species were recorded using NO_x–Ecotech EC9841, CO–Ecotech EC9830, and O₃–Ecotech EC9810 instruments
55 (PI: Cho Seogu) during the KORUS–AQ period (10 May 01:00:00 to 18 June 00:00:00 LT). As Olympic Park station has four
56 proximal NIER stations within 5 km, reproducing this research station data from the NIER interpolation should be a test of the
57 small scale variability of Seoul pollution provided the instruments are well calibrated.



58 **2.2.2 Taehwa Forest**

59 The Taehwa Forest wilderness site lies 30 km southeast of Olympic Park at 37.3123°N, 127.3105°E and at 200 m elevation
 60 (blue star in Fig. 1). It was used primarily to investigate the mixing of urban Seoul pollution with the biogenic volatile organic
 61 compounds (BVOCs) of the forest. The three key species were measured by the existing NIER instruments (PI: Youngjae Li),
 62 but supplemented by a Thermo Scientific 42i instrument for NO and a Cavity Ring–Down Spectroscopy for NO₂ (PI: Kim
 63 Saewung, Kim et al., 2022).



64 **Figure 1: (Left)** The geographical distribution of NIER ground stations and the two surface research stations operating during
 65 the KORUS–AQ campaign. High–precision stations (white circles) recorded CO at 1 ppb precision; low–precision stations
 66 (grey circles) recorded CO at 100 ppb increments. **(Right)** *Effective NIER station density (colour) within a 10 km radius* (see
 67 Eq. (3)) gridded over 0.1°x0.1° cells. The number of contiguous DC–8 flight transects through each box in the PBL is
 68 printed in each cell. The aircraft radar altitude was evaluated against the ERA5 PBL height (based on hourly 0.25°x0.25°
 69 gridded data, Hersbach et al., 2023). The ERA5 data was interpolated in time to match the aircraft data.

71 **2.3 NASA DC–8**

72 The DC–8 aircraft routinely profiled the air over Taehwa Forest via loop manoeuvres in the morning and afternoon on flight
 73 days between 2 May 2016 and 11 June 2016. It sampled other regions above South Korea and the Yellow Sea according to
 74 pollution plume transport and cloud forecasts. We use the 10 s merged data our three key species: O₃, NO, and NO₂ were
 75 measured with a 4–channel chemiluminescence instrument (Weinheimer et al., 1994); and CO, by Differential Absorption



76 Carbon monOxide Measurement (DACOM) (Sachse et al., 1991). We also use the 10 s data for latitude, longitude, radar
 77 altitude, UTC time, and potential temperature (PI: Melissa Yang). From the DC–8 potential temperature measurements and
 78 ERA5 surface data (Fig. A1) we can show that the ERA5 PBL heights accurately select DC–8 observations that are
 79 adiabatically mixed from the surface (i.e., $d\theta/dz \sim 0$), which is confirmed by the afternoon O_3 and CO profiles (Fig. A2). To
 80 determine when the aircraft was in the PBL and thus could be compared with the interpolated surface map, we use the ERA5
 81 PBL height data from reanalysis (hourly, $0.25^\circ \times 0.25^\circ$ grid, Hersbach et al., 2023). This approach is more accurate than simply
 82 assuming that all DC–8 observations below 1.5 km radar altitude fall within the PBL (e.g., Oak et al., 2019).

83 3 Methods

84 Interpolation techniques compute an objective estimate $\hat{f}(x)$ of a field $f(x)$ at any geographic location x and time t as
 a
 85 weighted mean of observations f_k at stations indexed by k with weights w_k :

$$86 \quad \hat{f}(x) = \frac{\sum_k w_k f_k}{\sum_k w_k} \quad (1)$$

87 Ordinary Kriging and Inverse Distance Weighting (IDW) are two common interpolation methods that operate by this premise
 88 but differ in how the station weights (w_k) are calculated (Matheron, 1963; Shepard, 1968). Kriging is a family of statistical
 89 techniques based on the supposition that phenomena are autocorrelated in space, relying on an empirical distance–based
 90 covariance model of $f(x)$ determined from the station data. In our work we find minimal correlation between ground station
 91 separation and covariance for any of the key species, so we opt for the modified IDW approach of Schnell et al. (2014).

92 3.1 Inverse Distance Weighting

93 In IDW techniques, weights are calculated from the reciprocal distances between estimation point x and the station coordinates
 94 x_k , scaled by the exponent β . The greater density of observations in some regions creates a source of oversampling bias.
 95 Schnell et al. (2014) address this clustering effect by reducing all station weights by n_k , the number of other stations within
 96 distance r_k of site x_k . In order to smooth the spatial heterogeneity in $\hat{f}(x)$ at small length scales, the distance r_k also
 serves
 97 as the minimum cutoff of r_k , and hence determines the maximum weighting w_k of any nearby station. L is a maximum
 98 cutoff of r_k used to reduce excess calculations for extremely distant and unimportant sites. The weight formulae are
 99 summarized in Eq. (2):

$$100 \quad w_k = \frac{1}{M_k} \quad r_k - r_c \leq r$$

$$101 \quad w_k = \frac{1}{M_k} \quad r_c < r_k - r_c \leq r \quad (2)$$



103

$$y_k(t) = 0$$

$$y_k(t) > 0$$

104

Our NIER station data consists of $k \in \{1, 2, \dots, 323\}$ locations (Fig. 1) and $t \in \{1, 2, \dots, 936\}$ hourly observations (10 May 01:00:00 to 18 June 00:00:00 LT) for each of our three key species (O_3 , CO, NO_x) with some unreported or erroneous data.

105

We optimize β and α for each key species k by randomly removing a fifth of the stations from the algorithm and then predicting



the abundance at each missing station k' . In minimizing the total root-mean-square error between predictions $\hat{y}_k(t)$ and observations $y_k(t)$ over the time series, we find similar optimal values for each species ($\beta \sim 2$ for O_3 , $\beta \sim 8$ for CO , and $\beta \sim 14$ for NO_x) with no significant improvement for larger β . We find similar optimal values for each species ($\beta \sim 2$ for O_3 , $\beta \sim 8$ for CO , and $\beta \sim 14$ for NO_x) with sites within a 10 km radius of k' in Eq. (3) (also called *Quality of Prediction*, Eq. (9) of Schmel et al., 2014). We expect β to correlate with prediction accuracy:

$$\beta \propto 10^\beta \sum_k y_k(t) \quad (3)$$

3.2 Statistical techniques

To evaluate the accuracy and predictive capability of an interpolation, we examine the error $\epsilon_1(t)$ in a time series of predictions $\hat{y}_k(t)$ and observations $y_k(t)$ at a given location for a given species with all time points equally weighted equally.

We

calculate a sequence of three error series defined as follows:

$$\begin{aligned} \epsilon_1(t) &= \hat{y}_k(t) - y_k(t) \\ \epsilon_2(t) &= \hat{y}_k(t) - \bar{y}_k - (\bar{\hat{y}}_k - \bar{y}_k) \\ \epsilon_3(t) &= \hat{y}_k(t) - \bar{y}_k - (\bar{\hat{y}}_k - \bar{y}_k) \end{aligned} \quad (4)$$

Where $\epsilon_1(t)$ is the absolute error in the predictions, $\epsilon_2(t)$ is the error after correcting for the mean prediction bias ($\bar{\hat{y}}_k - \bar{y}_k$) and $\epsilon_3(t)$ is the error relative to a simple linear regression (LR) model of $\hat{y}_k(t)$ vs. $y_k(t)$ fitted by ordinary least squares, i.e., after correcting for mean bias and slope ($\bar{\hat{y}}_k - \bar{y}_k$). We then apply the *coefficient of determination* to compute the fraction of the observed sample variance, $V(y_k(t))$, explained by e.g. the raw predictions ($\epsilon_1(t)$):

$$E_1 = 1 - \frac{V(\epsilon_1(t))}{V(y_k(t))} \quad (5)$$

And do similarly for $\epsilon_2(t)$ and $\epsilon_3(t)$. R_{E1}^2 is a *predictive accuracy* statistic that ranges from minus infinity to one and is identical to the forecast skill score referenced to the mean of observations (Murphy, 1988). R_{E2}^2 describes how well the predictions capture the temporal variability in the observations regardless of any mean bias and has the same range as R_{E1}^2 .

R_{E3}^2 is the common definition of R^2 in regression analysis and ranges from zero to one due to the fitting constraint. R_{E3}^2 describes the *predictability* of the observations from the LR model regardless of any difference in the mean or variance of $\hat{y}_k(t)$ and $y_k(t)$. A score of zero for a given β is equivalent to predicting a static mean of observations across the time R^2

domain. The maximum score for R_{E1}^2 and R_{E2}^2 is limited by the interpolation variance, which is typically damped relative to the contributing stations, especially in regions with highly heterogeneous emissions. Figure 2 (right-hand side) suggests the average station predictability (R_{E1}^2 and R_{E2}^2) score has an upper bound of around 0.9 for O_3 and 0.8 for CO and NO_x .



133 **3.2 Leave-one-out cross validation**

134 In this trial, we sequentially remove each station x_i , then interpolate (predict) its value from the remaining stations: x_1, x_2, \dots, x_n

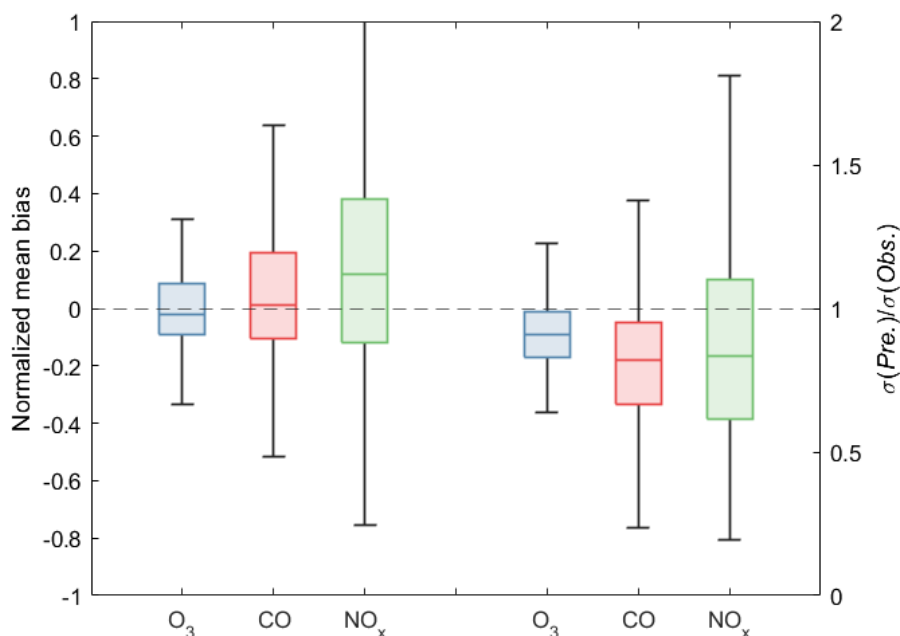
135 $\hat{x}_i =$

136 $\hat{x}_i(x_1, \dots, x_n)$, where $\hat{x}_i(x_1, \dots, x_n) = \hat{x}_i(x_1, \dots, x_n)$ (see Eq. (4); Brauer et al, 2003; Hochadel et al., 2006). A perfect interpolation would

accurately reproduce the mean and standard deviation of the measurements, indicating (1) no mean bias error and (2)



137 preservation of daily maximae and minimae. Our optimized IDW interpolation has clearly worked well in terms of mean bias
 138 (left half of Fig. 2). The box quartiles and non-outlier whiskers (i.e., the full range of values within one-and-a-half
 139 interquartile ranges from the outer quartiles) are well centred on zero bias, with the spread broadening from O₃ to CO to NO_x.
 140 The symmetry of the whiskers comes from the case where two sites, distant from the remaining sites but near one another, are
 141 the only sites used to interpolate one another and hence if one site has twice the mean value of another, we get symmetric plus-
 142 minus biases for each site. The median of the mean NO_x site biases is +13%, and this appears to be an artefact of low NO_x
 143 abundances in rural ($\rho < 5$) locations. The absolute mean NO_x bias averages -0.6 ppb (urban -3.0 ppb, rural +6.5 ppb).
 144 Incoherence among nearby urban stations combines to dampen the interpolation variability, especially for CO and NO_x, which
 145 feature independent high spatial variability from local sources. This is shown on the right half of Fig. 2, where most of the
 146 standard deviation ratio quantiles lie below unity. We believe this reduced standard deviation in the prediction time series
 147 better represents the average over a grid cell that contains several incoherent sites.



148 **Figure 2: (left)** Box plots of normalized mean bias: $\frac{\sum_{i=1}^n (x_i - \bar{x})}{n \cdot \bar{x}}$ and **(right)**
 149 standard deviation ratio $\frac{\sigma(\text{Pre.})}{\sigma(\text{Obs.})}$ for interpolated time series at each NIER site using leave-
 150 one-out cross
 151 validation. Whiskers show the range of non-outliers, where outliers are data beyond one-and-a-half interquartile ranges from
 152 the outer quartiles. Results are shown for O₃ (blue), CO (red), and NO_x (green). Mean bias is normalized by the observed mean,
 153 and the ratio of standard deviations is analogous to the gradient of a linear regression.

155 The sequence of R²_E scores (E1–3) for each site and each species are shown in Figure 3. The O₃ scores (top row) are consistently

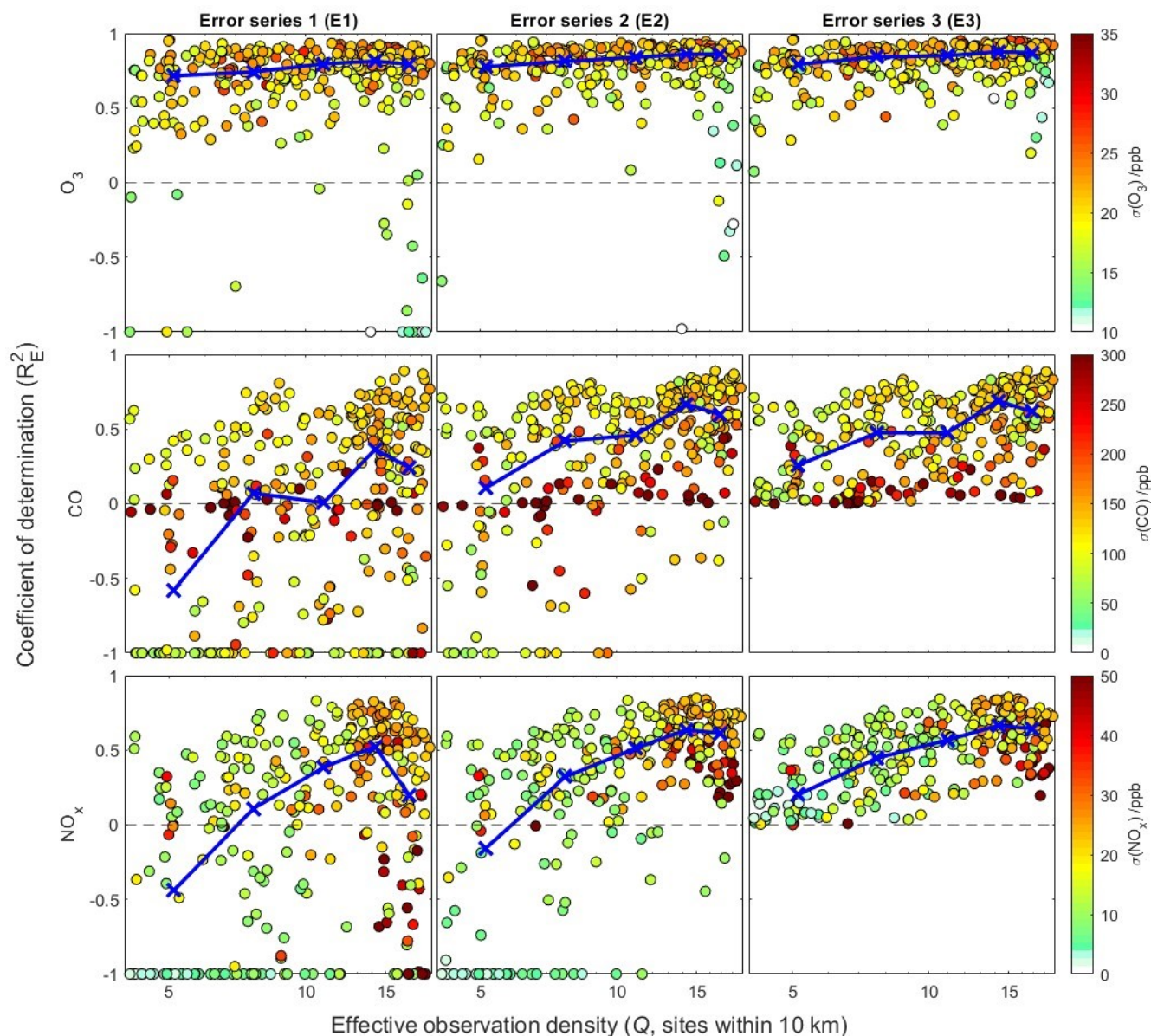


156 high across the sequence. R^2_{E1} through R^2_{E3} scores for O_3 indicate that the O_3 interpolation was accurate and unbiased at almost
157 all NIER stations in South Korea. For CO (middle row) and NO_x (bottom row), there is an improvement in absolute prediction



158 accuracy (R^2_{E1}) as the density of observations (\diamond) increases, and further improvement after correcting the mean bias in the
159 predictions (R^2_{E2}). The linear regression models (R^2_{E3}) offer an obvious improvement to predictability in rural regions (low \diamond)
160 where information is lacking, but no significant improvement in well sampled urban regions (high \diamond). With no large net mean
161 bias for any key species (Fig. 2), we assert that the average of our interpolations should capture the mean and possibly the
162 variability of a well-mixed gridded domain. We test this assertion later using aircraft PBL observations averaged into $0.1^\circ \times 0.1^\circ$
163 cells. The high range of R^2_E values for NO_x and CO, even where $\diamond > 10$, suggests that absolute mean error in the prediction is
164 a problem for many sites, implying they are driven by very small scale (<1 km) local emissions. For NO_x , the sequence to $E2$
165 and $E3$ greatly improves the prediction accuracy. For CO, there remains a large fraction of unpredictable sites, often with very
166 high standard deviations (dark red circles), implying large nearby emissions. Figure A3 (middle and right panels) shows the
167 clustering of such sites for CO and NO_x in Daejeon (central-western South Korea) and in the southern coastal cities of
168 Gwangyang, Yeosu, Suncheon, Jiju, and Ulsan (no NO_x data), possibly explained by high industrial activity in the coastal
169 cities.

170 We have additionally compared the interpolation accuracy during the four meteorological phases presented by
171 Peterson et al. (2019), i.e., dynamic, stagnant, low-level transport, and rex blocking. O_3 showed no significant difference across
172 the phases, while NO_x seemed slightly more predictable by our metrics during the dynamic and stagnant weather phases. CO
173 predictability improved slightly during the stagnant phase only.



174

175 **Figure 3:** Generalized coefficient of determinations (R^2_E Eq. (5)) for NIER station predictions vs. the effective density of
 176 nearby observations (Q , effective number of sites in a 10 km radius). The three columns show the sequence R^2_{E1} , R^2_{E2} and
 177 R^2_{E3} . The three rows are for the species O₃ (**top**), CO (**middle**), and NO_x (**bottom**). The calculations use the leave-one-out
 178 cross validation at each NIER station (circles) coloured by the standard deviation of observations. The blue conjoined crosses
 179 show the median R^2_E values for five percentile partitions of Q : 0–20%, 20–40%, 40–60%, 60–80%, and 80–100%.

180 3.3 Gridded air quality data

181 A major objective of this study was to obtain grid-cell averages (0.1°x0.1°, approx. 10 km x 10 km) for testing regional air
 182 quality models. Within each 0.1°x0.1° cell, we interpolate the key species to twenty five points on a 0.02°x0.02° grid centred



183 in the cell, and then average these values. The averages do not account for latitudinal differences in quadrangle areas, which
 184 are minor for South Korean latitudes. We apply the same treatment to the density of observations to produce the gridded Q
 185 values as seen in Fig. 1B.

186 3.4 Aircraft cell averages

187 We collect the measurements of O_3 , CO , and NO_x from NASA DC-8 taken over land at radar altitudes below the PBL heights
 188 taken from the ERA5 data. The DC-8 measurements used here are 10 second merges corresponding to approximately 1 km
 189 flight segments $\in \{1, 2, \dots, 13942\}$. To compare the segments with the gridded site data, we average the contiguous
 190 segments through each grid cell producing transect-averaged observations $\{O_3, CO, NO_x\}$. For the prediction set $\{O_3, CO, NO_x\}$, we interpolate the
 191 traversed cells in time to match the mean aircraft time of flight during the respective transects. The number of transects through
 192 each cell is indicated by the gridded numbers in Fig. 1B.

194 4 Results

195 **Table 1:** The generalized coefficients of determination R^2_{E1} , R^2_{E2} , and R^2_{E3} (Eq. (5)) for predictions vs. measurements at
 196 research stations (Olympic Park and Taehwa Forest) and along flight transects in the PBL. Each flight transect is a median of
 197 contiguous 10 s observations through a grid cell (See Fig. 1 for sampling distribution and Fig. 4 for scatter plots), and the
 198 predictions are gridded values interpolated linearly in time to match the aircraft time of flight, then averaged. $E1$, $E2$, and $E3$
 199 are time series of prediction errors defined in Eq. (4). NO_x measurements at Taehwa Forest are taken from Kim et al., 2022.
 200

	Olympic Park			Taehwa Forest			DC-8 (all transects)			DC-8 ($Q > 10$ transects)		
Species	R^2_{E1}	R^2_{E2}	R^2_{E3}	R^2_{E1}	R^2_{E2}	R^2_{E3}	R^2_{E1}	R^2_{E2}	R^2_{E3}	R^2_{E1}	R^2_{E2}	R^2_{E3}
O_3	0.90	0.92	0.96	0.68	0.82	0.82	0.02	0.69	0.69	0.26	0.81	0.90
CO	0.73	0.75	0.76	-2.70	0.69	0.71	-2.20	0.28	0.41	-0.91	0.83	0.84
NO_x	0.67	0.68	0.68	-12.0	-3.60	0.00	-2.60	0.34	0.62	-0.84	0.51	0.73

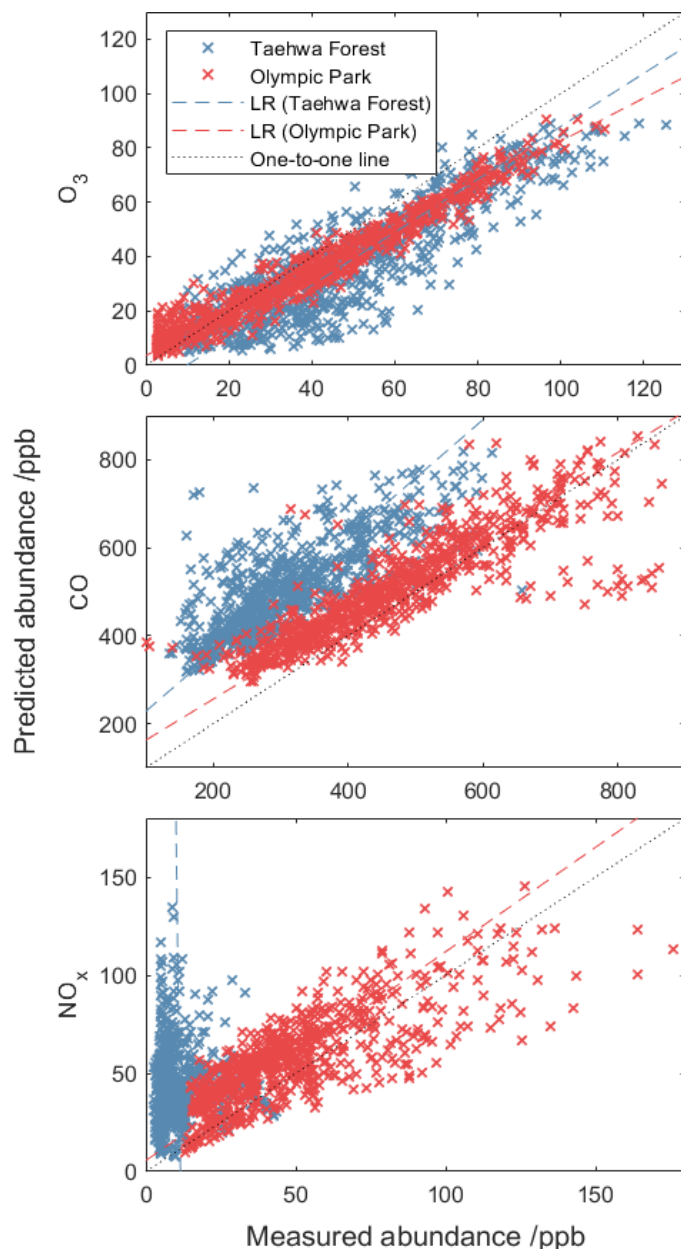
201 4.1 Research site prediction

202 Research stations provide case studies where the quality of measurements is carefully controlled, and so instrumental drift,
 203 noise, and biases are minimized. For each key species, we compare the NIER station data interpolated to the coordinates of
 204 the research stations, either at Olympic Park or Taehwa Forest, against the research station instruments (Fig. 4). Olympic Park
 205 and Taehwa Forest have effective sampling densities ρ of 16 and 6 stations per 10 km respectively. Figure 4 shows accurate
 206 prediction of O_3 at both sites with predictably more scatter at Taehwa Forest where less information was available. We see a
 207 similar pattern for CO , but with a mean bias (predicted NIER interpolated value minus research instrument measurement) of
 208 +100 ppb at Taehwa Forest. NO_x is predicted reasonably well at Olympic Park except in the highest measured range (>100



209 ppb), but predictions appear random at Taehwa Forest. Table 1 indicates excellent prediction accuracy at Olympic Park for all
210 species (R^2_{E1}), and at Taehwa Forest for O_3 . At Taehwa Forest, CO prediction improves when mean biases are removed (R^2_{E2}),
211 but NO_x remains unpredictable. The linear regressions (R^2_B) lead to very little improvement over mean bias correction (R^2_E),
212 implying that the temporal variability measured by the research stations was well captured. High R^2_{E1} scores suggest good co-
213 calibration between the Olympic Park instruments and surrounding NIER instruments. We are unable to characterize the mean
214 biases at Taehwa Forest.

215 As an isolated wilderness site, Taehwa Forest presents a unique problem for interpolating NO_x values based on NIER
216 stations. The closest three NIER sites surround the forest station at a distance of around 10–15 km, and all are subject to NO_x
217 roadside emissions, thus our interpolation maps these high- NO_x values into the relatively NO_x -depleted forest.



218

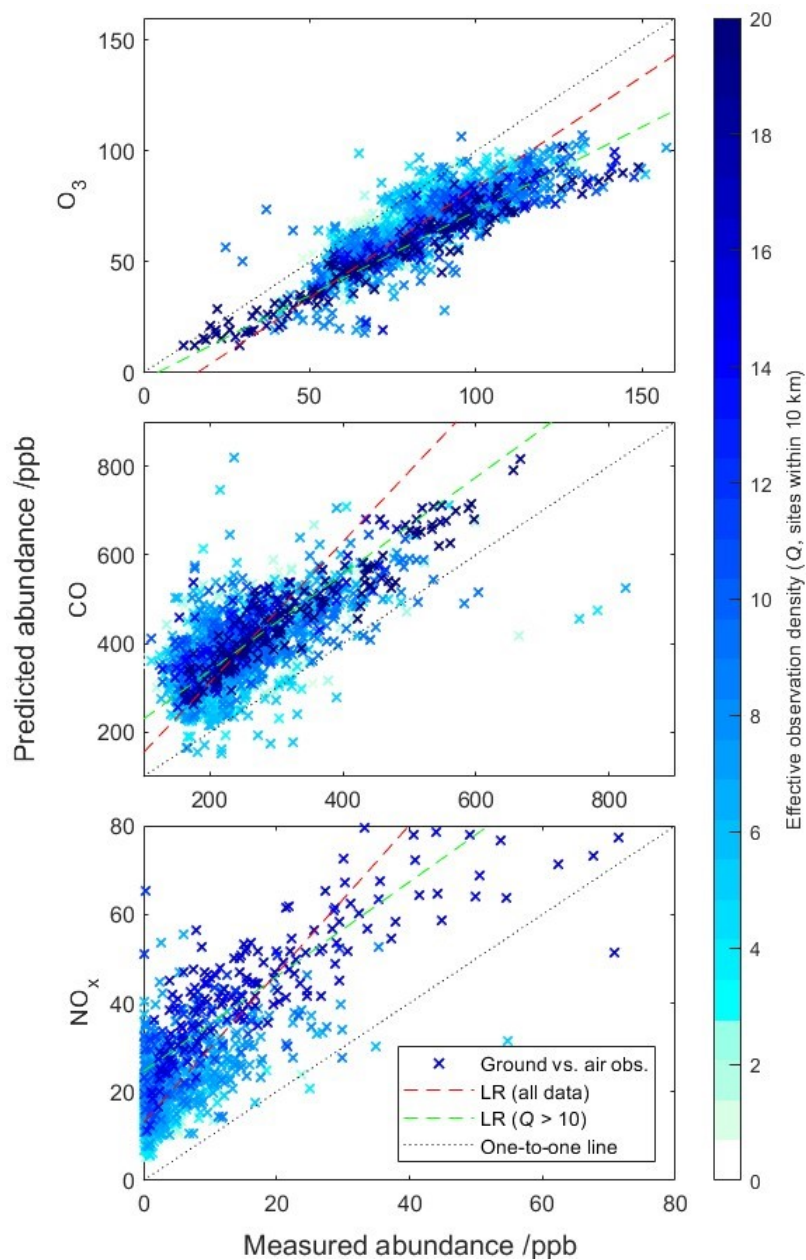
219 **Figure 4:** Predicted vs. measured abundances of the three key species at Olympic Park (red) and Taehwa forest (blue) research
220 stations. Predicted abundances are computed as point interpolations as per Equation (1). Dashed lines are linear regression
221 (LR) models fitted by ordinary least squares.

222 4.2 DC-8 comparison

223 Figure 5A shows that the gridded surface-site predictions of the DC-8 O_3 observations are consistently lower than observed
224 but remain strongly correlated. CO predictions (Fig. 5B) show a consistent bias of around +100 ppb, but otherwise capture the



225 variability of the aircraft CO measurements reasonably well. NO_x predictions (Fig. 5C) show a consistent positive bias along
226 with randomness in the low measured range (<10 ppb). The gridded O₃ and CO predictions are highly accurate ($R^2_{E2} = 80\%$)
227 in grid cells with effective observation density (Q) exceeding ten, mainly sampled in the Seoul Metropolitan Area (Fig. 1B).
228 These findings show that with enough ground information, our gridded O₃ and CO datasets can predict upper PBL variability
229 even in regions with intense small-scale emission heterogeneity. NO_x is exceptional, however, due to the rapid falloff in
230 abundance with altitude even within the PBL (Fig. A3 of Appendix A, see also Fig. 2 from Kim et al., 2021). O₃ titration in
231 the Seoul Metropolitan Area also leads to a slight underestimation in predicted variability, shown by a 10% increase in
232 predictability using linear regression ($R^2_{E3} = 90\%$, Table 1). Obtaining vertically averaged concentrations rather than surface
233 values remains a challenge given the substantial near-surface gradients inferred from Figures 5 and A2, and suggests the need
234 for vertically resolved chemical and dynamical modelling.



235

236

237

238

Figure 5: Comparison of 10 s DC-8 observations in the PBL and gridded ($0.1^\circ \times 0.1^\circ$) hourly ground station data. Each data point represents the median of the contiguous aircraft transect through a grid cell (y -axis) and the median of the gridded ground station data interpolated linearly in time to match the aircraft time of flight (x -axis).



239 **5 Conclusions**

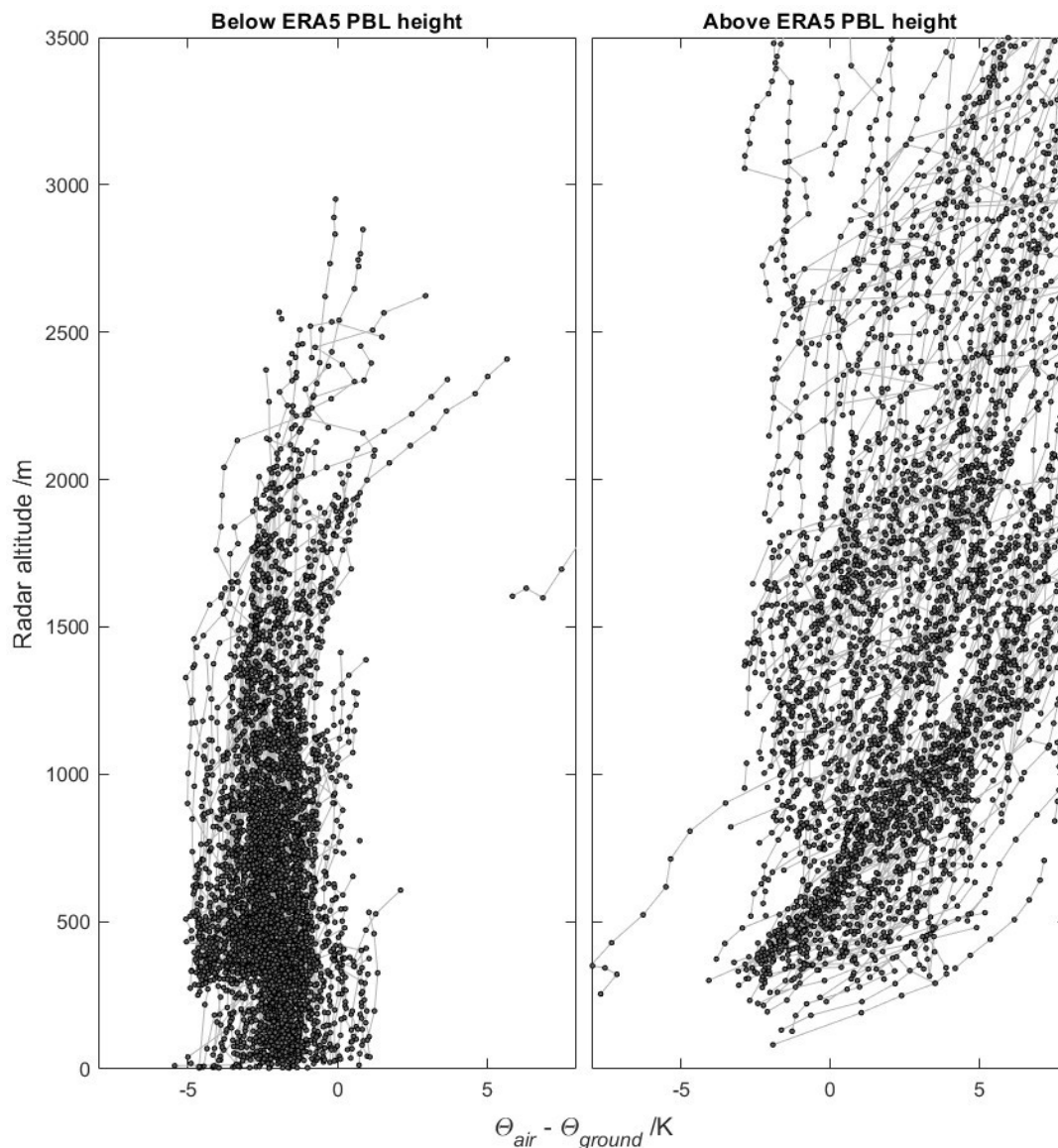
240 We create gridded ($0.1^\circ \times 0.1^\circ$) observational datasets from NIER ground station measurements of air quality over South Korea.
241 The method includes information from all nearby stations, including those outside of the cell boundary, while also mitigating
242 sampling bias from site clustering. Our results suggest that the mean and variability of ground level O_3 is well captured over
243 the whole of South Korea. For CO and NO_x , our leave-one-out cross validation revealed mean biases in certain NIER site
244 predictions, but otherwise good prediction accuracy in most densely observed urban regions after the biases were subtracted.
245 The well predicted regions include the Seoul Metropolitan Area, Busan, Changwon, Daegu, and Cheongju, whereas prediction
246 accuracy was poor in the conjoined coastal cities of Gwangyang, Yeosu, and Suncheon, and in Ulsan. The aircraft comparisons
247 confirm that the variability of O_3 and CO in the PBL are well captured from the surface stations; however, NO_x vertical
248 gradients in the PBL confound attempts to predict the aircraft NO_x measurements.

249
250
251
252
253
254
255
256
257
258
259
260
261
262
263
264
265
266
267
268
269



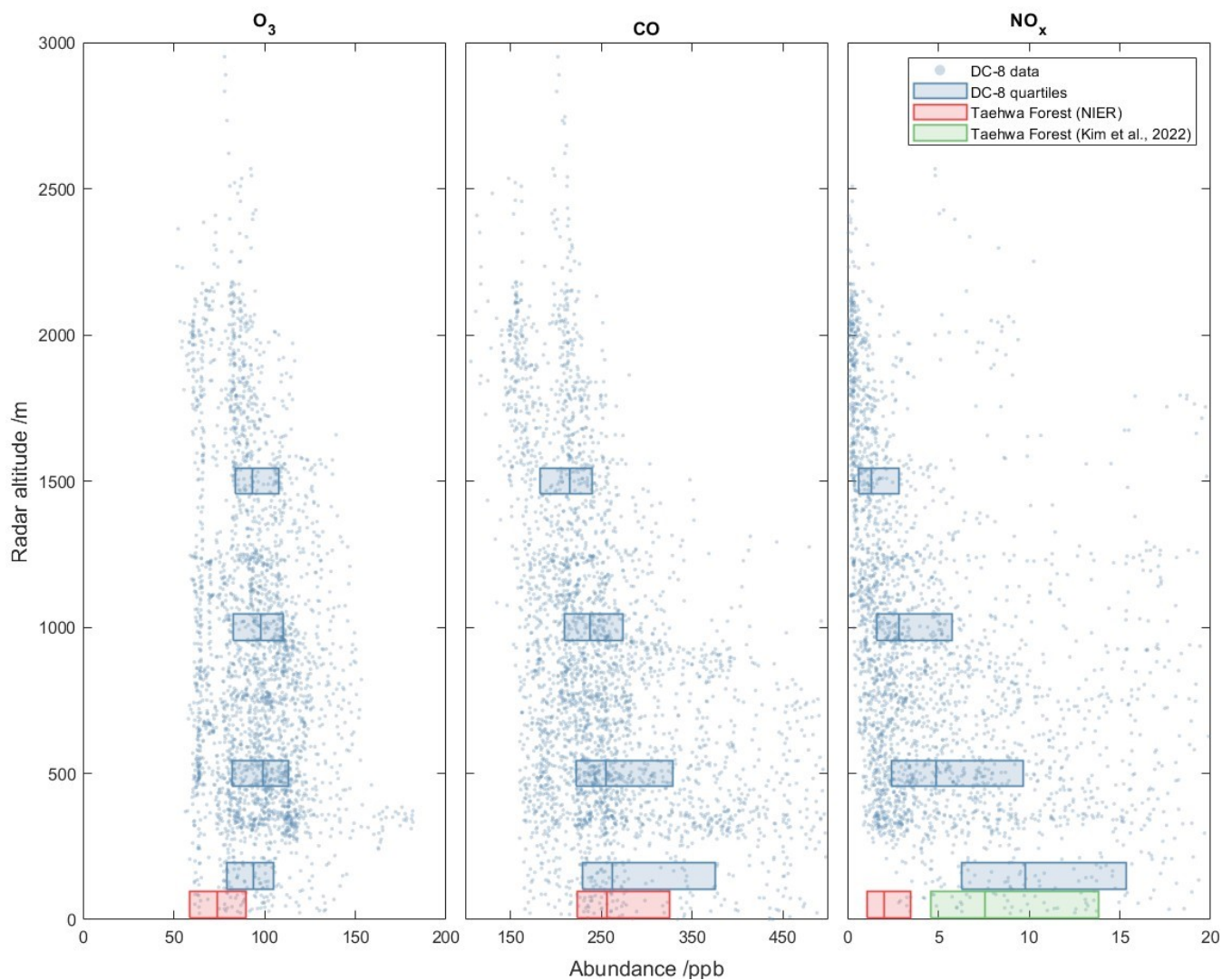
270 **6 Appendices**

271 Appendix A



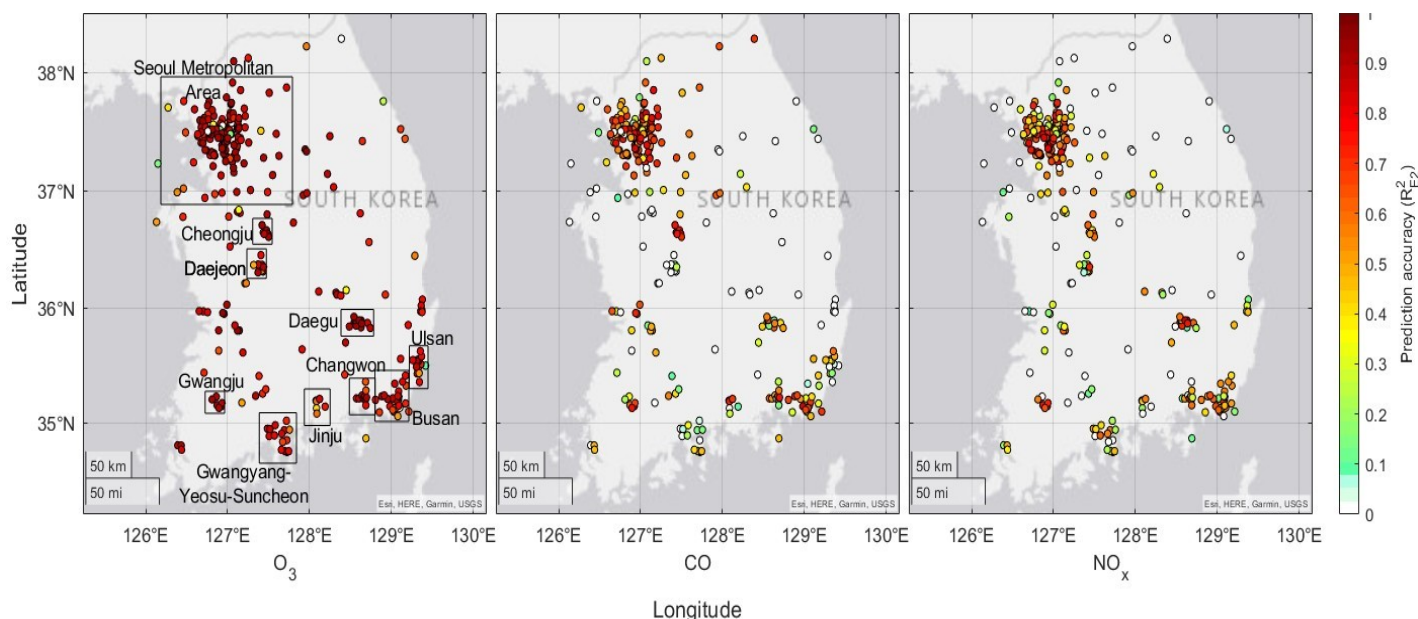
272

273 **Figure A1:** DC-8 10 s potential temperature (θ_{air}) measurements (dots) in a half degree radius of Taehwa Forest research
274 station with gridded ($0.25^\circ \times 0.25^\circ$) surface potential temperature (θ_{ground}) subtracted, taken below (**left**) and above (**right**) the
275 ERA5 designated PBL height. Lines connecting dots indicate contiguous transects, and all data was taken during ascent or
276 descent (aircraft vertical speed $> 1 \text{ m s}^{-1}$). θ_{ground} was calculated using the ERA5 2 metre temperature and surface pressure
277 fields at native resolution ($0.25^\circ \times 0.25^\circ$, hourly), interpolated in time to match the aircraft time of flight.
278



279
280
281
282
283

Figure A2: Vertical profiles of the DC-8 measured O₃ (**left**), CO (**middle**), and NO_x (**right**) in the ERA5 PBL within a half degree radius of Taehwa Forest research station. All data is sampled between the hours of 12:00 and 17:00 LT, and quartiles are shown for aircraft data (blue) partitioned into altitude bins (0–250, 250–750, 750–1250, and 1250–1750 m) and for the available ground research station measurements at Taehwa Forest (red) supplemented by Kim et al., 2022 (green).



284

Figure A3: The geographical distribution of NIER station prediction accuracies with the mean prediction bias removed from each station (R^2_{E2} , Eqs. (4) and (5)), shown for the three key species: O_3 (left), CO (middle), and NO_x (right). Negative R^2_{E2} values are truncated to zero. Cities are shown by text and boxes in the O_3 panel, including the approximate bounds of the Seoul Metropolitan Area.

289 **Data Availability**

290 Gridded data products and the datasets used in analysis are available from Wilson, 2024:

291 <https://doi.org/10.5061/dryad.sf7m0cgf5>.

292 **Author contribution**

293 CW wrote the code to produce the datasets, codesigned and performed the analysis, and prepared the manuscript. MP designed the methodology, codesigned the analysis, reviewed and edited the manuscript.

295 **Competing interests**

296 The authors declare that they have no conflict of interest.



297 **Acknowledgements**

298 This study was funded by NASA (# 80NSSC21K1454) and the National Science Foundation (NSF, # AGS-2135749). We
299 acknowledge NASA and NIER for providing the trace gas data used in this study and we are grateful to Kim Saewung for
300 guidance on the KORUS-AQ data usage.

301 **References**

- 302 Brauer, M., Hoek, G., van Vliet, P., Meliefste, K., Fischer, P., Gehring, U., Heinrich, J., Cyrys, J., Bellander, T., Lewne, M.,
303 & Brunekreef, B.: Estimating Long-Term Average Particulate Air Pollution Concentrations: Application of Traffic Indicators
304 and Geographic Information Systems. *Epidemiology*, 14 (2), 228–239, 10.1097/01.EDE.0000041910.49046.9B, 2003.
- 305 Crawford, J., Ahn, J., Al-Saadi, J., Chang, L., Emmons, L., Kim, J., Lee, G., Park, J., Park, R., Woo, J., Song, C., Hong, J.,
306 Hong, Y., Lefer, B., Lee, M., Lee, T., Kim, S., Min, K., Yum, S., Shin, H., Kim, Y., Choi, J., Park, J., Szykman, J., Long, R.,
307 Jordan, C., Simpson, I., Fried, A., Dibb, J., Cho, S., and Kim, Y.: The Korea–United States Air Quality (KORUS–AQ) field
308 study. *Elementa: Science of the Anthropocene*, 9 (1): 00163. <https://doi.org/10.1525/elementa.2020.00163>, 2021.
- 309 Eck, T.F., Holben, B.N., Kim, J., Beyersdorf, A.J., Choi, M., Lee, S., Koo, J. H., Giles, D. M., Schafer, J. S., Sinyuk, Peterson,
310 A. D. A., Reid, J. S., Arola, A., Slutsker, I., Smirnov, A., Sorokin, M., Kraft, J., Crawford, J. H., Anderson, B. E., Thornhill,
311 K. L., Diskin, G., Kim, S. W., Park, S. J.: Influence of cloud, fog, and high relative humidity during pollution transport events
312 in South Korea: Aerosol properties and PM_{2.5} variability, *Atmos. Environ.*, 232,
313 <https://doi.org/10.1016/j.atmosenv.2020.117530>, 2020.
- 314 Hochadel, M., Heinrich, J., Gehring, U., Morgenstern, V., Kuhlbusch, T., Link, E., Wichmann, H. E., Krämer, U.: Predicting
315 long-term average concentrations of traffic-related air pollutants using GIS-based information, *Atmos. Environ.*, 40, 542–
316 553, <https://doi.org/10.1016/j.atmosenv.2005.09.067>, 2006.
- 317 Hersbach, H., Bell, B., Berrisford, P., Biavati, G., Horányi, A., Muñoz Sabater, J., Nicolas, J., Peubey, C., Radu, R., Rozum,
318 I., Schepers, D., Simmons, A., Soci, C., Dee, D., Thépaut, J–N. (2023): ERA5 hourly data on single levels from 1940 to
319 present. Copernicus Climate Change Service (C3S) Climate Data Store (CDS), <https://doi.org/10.24381/cds.adbb2d47>
320 (Accessed on 28–02–2024).
- 321 Jordan, C., Crawford, J. H., Beyersdorf, A. J., Eck, T. F., Halliday, H. S., Nault, B. A., Chang, L. S., Park, J. S., Park, R. J.,
322 Lee, G. W., Kim, H. J., Ahn, J. Y., Cho, S. J., Shin, H. J., Lee, J. H., Jung, J. S., Kim, D. S., Lee, M. H., Lee, T. H., Whitehill,
323 A., Szykman, J., Schueneman, M. K., Campuzano–Jost, P., Jimenez, J. L., DiGangi, J. P., Diskin, G. S., Anderson, B. E.,
324 Moore, R. H., Ziemba, L. D., Fenn, M. A., Hair, J. W., Kuehn, R. E., Holz, R. E., Chen, G., Travis, K., Shook, M., Peterson,
325 D. A., Lamb, K. D., Schwarz, J. P.: Investigation of factors controlling PM_{2.5} variability across the South Korean Peninsula
326 during KORUS–AQ. *Elementa: Science of the Anthropocene*, 8, 28, <https://doi.org/10.1525/elementa.424>, 2020.
- 327 Kim, H., Park, R. J., Kim, S., Brune, W. H., Diskin, G. S., Fried, A., Hall, S. R., Weinheimer, A. J., Wennberg, P., Wisthaler,
328 A., Blake, D. R., and Ullmann, K.: Observed versus simulated OH reactivity during KORUS–AQ campaign: Implications for



- 329 emission inventory and chemical environment in East Asia. *Elementa: Science of the Anthropocene*, 10 (1), 00030,
330 <https://doi.org/10.1525/elementa.2022.00030>, 2022.
- 331 Kim, S., Seco, R., Gu, D., Sanchez, D., Jeong, D., Guenther, A., Lee, Y., Mak, J., Su, L., Kim, D., Lee, Y., Ahn, J., Mcgee,
332 T., Sullivan, J., Long, R., Brune, W., Thames, A., Wisthaler, A., Müller, M., Mikoviny, T., Weinheimer, A., Yang, M., Woo,
333 J., Kim, S., Park, H.: The role of a suburban forest in controlling vertical trace gas and OH reactivity distributions – a case
334 study for the Seoul metropolitan area, *Faraday Discuss.*, 226, 537–550, <https://doi.org/10.1039/D0FD00081G>, 2021.
- 335 Lennartson, E., Wang J., Gu J., L. C. Garcia, Ge C., Gao M., Choi M., Saide Peralta, G. Carmichael, Kim J., and Janz S.:
336 Diurnal variation of aerosol optical depth and PM_{2.5} in South Korea: a synthesis from AERONET, satellite (GOCI), KORUS–
337 AQ observation, and the WRF–Chem model, *Atmos. Chem. Phys.*, 18, 15125–15144, [https://doi.org/10.5194/acp-18-15125-](https://doi.org/10.5194/acp-18-15125-2018)
338 2018, 2018.
- 339 Matheron, G.: Principles of geostatistics, *Econ. Geol.*, 58 (8), 1246–1266, <https://doi.org/10.2113/gsecongeo.58.8.1246>, 1963.
- 340 Murphy, A. H.: Skill scores based on the mean square error and their relationships to the correlation coefficient, *Mon. Wea.*
341 *Rev.*, 116, 2417–2424, [https://doi.org/10.1175/1520-0493\(1988\)116<2417:SSBOTM>2.0.CO;2](https://doi.org/10.1175/1520-0493(1988)116<2417:SSBOTM>2.0.CO;2), 1988.
- 342 Oak, Y. J., Park, R. J., Schroeder, J. R., Crawford, J. H., Blake, D. R., Weinheimer, A. J., Woo, J., Kim, S., Yeo, H., Fried, A.,
343 Wisthaler, A., and Brune, W. H.: Evaluation of simulated O₃ production efficiency during the KORUS–AQ campaign:
344 Implications for anthropogenic NO_x emissions in Korea, *Elementa: Science of the Anthropocene*, 7, 56,
345 <https://doi.org/10.1525/elementa.394>, 2019.
- 346 Park, R. J., Oak, Y. J., Emmons, L. K., Kim, C. H., Pfister, G. G., Carmichael, G. R., Saide, P. E., Cho, S., Kim, S., Woo, J.,
347 Crawford, J. H., Gaubert, B., Lee, H., Park, S., Jo, Y., Gao, M., Tang, B., Stanier, C. O., Shin, S., Park, H., Bae, C., and Kim,
348 E.: Multi–model intercomparisons of air quality simulations for the KORUS–AQ campaign. *Elementa: Science of the*
349 *Anthropocene*, 9 (1), 00139, <https://doi.org/10.1525/elementa.2021.00139>, 2021.
- 350 Peterson, D. A., Hyer, E., Han, S., Crawford J., Park, R. J., Holz, R., Kuehn, R. E., Eloranta, E., Knote, C. J., Jordan, C. E.,
351 and Lefer, B.: Meteorology influencing springtime air quality, pollution transport, and visibility in Korea, air quality, pollution
352 transport, and visibility in Korea. *Elem Sci*, 7, 57, <https://doi.org/10.1525/elementa.395>, 2019.
- 353 Sachse, G. W., Collins, J. E. Jr., Hill, G. F., Wade, L. O., Burney, L. G., and Ritter, J. A.: Airborne tunable diode laser sensor
354 for high–precision concentration and flux measurements of carbon monoxide and methane. In *Measurement of atmospheric*
355 *gases 1433: 157–166*. International Society for Optics and Photonics, <https://doi.org/10.1117/12.46162>, 1991.
- 356 Schnell, J. L., Holmes, C. D., Jangam, A., and Prather, M. J.: Skill in forecasting extreme ozone pollution episodes with a
357 global atmospheric chemistry model, *Atmos. Chem. Phys.*, 14, 7721–7739, <https://doi.org/10.5194/acp-14-7721-2014>, 2014.
- 358 Schroeder, J. R., Crawford, J. H., Ahn, J. Y., Chang, L. S., Fried, A. Walega, J. Weinheimer, A., Montzka, D. D., Hall, S. R.,
359 Ullmann, K., Wisthaler, A., Mikoviny, T., Chen, G., Blake, D. R., Blake, N. J., Hughes, S. C., Meinardi, S., Diskin, G.,
360 Digangi, J. P., Choi, Y. H., Pusede, S. E., Huey, G. L., Tanner, D. J., Kim, M., Wennberg, P.: Observation–based modeling of
361 ozone chemistry in the Seoul metropolitan area during the Korea–United States Air Quality Study (KORUS–AQ). *Elementa:*
362 *Science of the Anthropocene*, 8, 3, <https://doi.org/10.1525/elementa.400>, 2020.



- 363 Shepard, S.: A two-dimensional interpolation function for irregularly-spaced data, in: Proceedings of the 1968 23rd ACM
364 national conference (ACM '68), Association for Computing Machinery, New York, NY, USA, 517–524,
365 <https://doi.org/10.1145/800186.810616>, 1968
- 366 Susaya, J., Kim, K., Shon, Z., and Brown, R.: Demonstration of long-term increases in tropospheric O₃ levels: Causes and
367 potential impacts, *Chemosphere*, 92, 1520–1528, <https://doi.org/10.1016/j.chemosphere.2013.04.017>, 2013.
- 368 Travis, K. R., Crawford, J. H., Chen, G., Jordan, C. E., Nault, B., Kim, H., Jimenez, J. L. Jost, C., Dibb, J., Woo, J. H., Kim,
369 Y., Zhai, S., Wang, X., McDuffie, E., Luo, G., Yu, F., Kim, S., Simpson, I. J., Blake, D. R., Chang, L., Kim, M. J.: Limitations
370 in representation of physical processes prevent successful simulation of PM_{2.5} during KORUS–AQ, *Atmos. Chem. Phys.*,
371 <https://doi.org/10.5194/acp-22-7933-2022>, 2022.
- 372 Weinheimer, A. J., Walega, J. G., Ridley, B. A., Gary, B. L., Blake, D. R., Blake, N. J., Rowland, F. S., Sachse, G. W.,
373 Anderson, B. E., and Collins, J. E.: Meridional distributions of NO_x, NO_y, and other species in the lower stratosphere and
374 upper troposphere during AASE II., *Geophys. Res. Lett.*, 21 (23), 2583–2586, <https://doi.org/10.1029/94GL01897>, 1994.
- 375 Wilson, C.: KORUS-AQ gridded O₃, NO_x, and CO observations created using ground station data, Dryad [data set],
376 <https://doi.org/10.5061/dryad.sf7m0cgf5>, 2024.